Peer-reviewed version available at *Materials* **2018**, *12*, 7; doi:10.3390/ma12010007

Article

A three phase model charactering low-velocity impact response of SMA reinforced composites under vibrating boundary condition

Mengzhou Chang [1], Fangyun Kong [1], Min Sun [1] and Jian He [1,*]

[1] College of Aerospace and Civil Engineering, Harbin Engineering University, Harbin 150001, China; changmengzhou@hrbeu.edu.cn; kongfangyun@hrbeu.edu.cn; sunmin@hrbeu.edu.cn

* Correspondence: hejian@hrbeu.edu.cn; Tel.: +86 0451 8252 5056

Abstract: Structural vibration induced by dynamic load or natural vibration is a nonnegligible factor in failure analysis. Based on vibrating boundary condition, impact resistance of shape memory alloy reinforced composites is investigated. In this investigation, modified Hashin's failure criterion, Brinson's model and visco-hyperelastic model are implemented into the numerical model to charactering the mechanical behavior of glass fiber/epoxy resin laminates, SMAs and interphase, respectively. First, fixed boundary condition is maintained in simulation to verify the accuracy of material parameters and procedures by comparing with experimental data. Then, a series of vibrating boundaries with different frequencies and amplitudes are applied during the simulation process to reveals the effect on impact resistances. The statistics of absorbed energy and contact force indicate that impact resistance of the composite under high frequency and large amplitude is lower than that under low frequency and small amplitude, and summarized by a mathematical expression.

Keywords: SMA reinforced composite; low-velocity impact; vibrating boundary; numerical analysis

1. Introduction

Fiber reinforced composite materials have been widely used and investigated in recent years due to their unique properties, such as high stiffness, high strength and low density [1]. However, the applications of the composites are limited by their weak impact resistance, especially for the unidirectional cross-ply fiber/matrix laminates. Obviously, the reason for this disadvantage can be traced to the low strength, stiffness between the adjacent layers which will result in delamination and fiber breakage [2].

This disadvantage can be overcome by changing the composition of material: for example, using short fiber instead of long fiber. The mechanical properties of short fiber reinforced composites are strongly influenced by the manufacturing process, such as injection position, sample geometry, pressure and temperature during the molding process [3-4]. Other factors, such as fiber location, length, diameter and orientation that affect the mechanical properties, have been studied by Thomason [5-7], Wang [8] and Mallick [9] investigate the tensile properties of composite machined with different angles to mould flow direction (MFD). The results indicate that tensile strength (and elastic modulus) of samples machined perpendicular to MFD are nearly 40% lower than that of samples machined parallel to MFD.

Functional materials and new structures have been used to improve the mechanical property of the composites. Shape memory alloys (SMAs) have been embedded between the adjacent layers for the reinforcement purpose considering their unique properties: changing shape (elastic modulus) in

Preprints (www.preprints.org) | NOT PEER-REVIEWED | Posted: 7 November 2018 doi:10.20944/preprints201811.0180.v1

Peer-reviewed version available at *Materials* **2018**, *12*, 7; doi:10.3390/ma12010007

accordance with temperature and stress [10-11]. In our previous research, the effect of SMAs positions on damage behavior and impact response (including peak force, displacement and energy) of laminates subjected to low-velocity impact have been investigated [12]. In Khalili's research, the effect of SMAs type (wires, plates, strips, tubes or layers) on dissipation of the impact energies has been studied [13-14]. According to Shariyat's research, a higher order global-local hyperbolic plate theory aimed at studying the asymmetric displacement fields has proposed, the related results indicate that SMAs have the ability to change shape, to repair damage and to improve impact property of composites [15-16]. The new structure bounding of the conventional fiber reinforced polymer with metal layer is also found has the advantage when subjecting to impact loading [17]. Other structures, such as particle reinforced [18-19], sandwich plate [20-21] and 3D fabric [22-23] have been developed in recent years.

We note that the fixed boundary is widely used in the experimental analysis. Except for low and high velocity impact, the mechanical properties of composite under eccentric impact [24], multi-impact [25] and compression-after-impact [26] has received much attention due to engineering practices. However, the vibrating boundary condition, which is unavoidable when membrane structures subjected to impact [27] or wind flow [28], has rarely discussed due to the difficulties associated with real experimental condition. Only vibration response during impact and after impact can be observed to evaluate the impact resistance and damage state [29-30]. In Pérez MA's work, damage of CFRP induced by low velocity impact and its effect on vibration response is investigated by a micro-mechanical approach [31].

The interfacial debonding between SMA and the matrix, one common failure model, is still a key problem in the composites [32]. As reported in our previous work, a three phase model-matrix, reinforcer and interphase is introduced to evaluating the mechanical behavior of fiber reinforced composite [33]. In this paper, this model is further developed to matching the SMA reinforced composites. Based on this model, the effect of vibration on impact resistance of SMAs reinforced composites is mainly investigated through a series of frequencies and amplitudes.

2. The three phase model

2.1. Material property of glass fiber reinforced composites

Glass fiber and the matrix used in this paper are regarded as homogeneous isotropic materials on microscale. The constitutive model can be expressed as:

$$\sigma_{ij}=2G\varepsilon_{ij}+\lambda\varepsilon_{kk}\delta_{ij} \tag{1}$$

where ε_{ij} and σ_{ij} are nominal strain and stress in case of $i=j$, shear strain and shear stress in case of $i \neq j$ ($i, j=$ x, y and z are the reference coordinates X), respectively. $\lambda= E\mu/(1+\mu)(1-2\mu)$ is the Lame's constant and $G=E/2(1+\mu)$ is the shear modulus, E and μ are the elastic modulus and Poisson's ratio, $\varepsilon_{kk}=\varepsilon_{xx}+\varepsilon_{yy}+\varepsilon_{zz}$ is the volumetric strain, δ_{ij} is the Kronecker delta ($\delta_{ij}=1$ if $i=j$, and $\delta_{ij}=0$ otherwise). The relationship between displacement field u_i and strain field ε_{ij} defined as:

$$\varepsilon_{ij}=\frac{1}{2}\left(\frac{\partial u_i}{\partial X_j}+\frac{\partial u_j}{\partial X_i}\right) \tag{2}$$

However, it's quite unrealistic modeling each glass fiber in ABAQUS considering the complexity. A ply including glass fiber and epoxy resin is modeled as anisotropic material. The stacking sequence is $[0°, 90°]_8$, and the total thickness of the sample is about 3.2 mm (0.2 mm for each ply). The related material parameters are obtained according to the experimental work of our research group [12], as shown in Table 1.

Peer-reviewed version available at Materials 2018, 12, 7; doi:10.3390/ma12010007

For the undamaged state, the stress strain relationship can be rewritten as:

$$\begin{Bmatrix} \sigma_{11} \\ \sigma_{22} \\ \sigma_{33} \\ \sigma_{23} \\ \sigma_{31} \\ \sigma_{12} \end{Bmatrix} = \begin{bmatrix} c_{11} & c_{12} & c_{13} & 0 & 0 & 0 \\ c_{21} & c_{22} & c_{23} & 0 & 0 & 0 \\ c_{31} & c_{32} & c_{33} & 0 & 0 & 0 \\ 0 & 0 & 0 & c_{44} & 0 & 0 \\ 0 & 0 & 0 & 0 & c_{55} & 0 \\ 0 & 0 & 0 & 0 & 0 & c_{66} \end{bmatrix} \begin{Bmatrix} \varepsilon_{11} \\ \varepsilon_{22} \\ \varepsilon_{33} \\ \varepsilon_{23} \\ \varepsilon_{31} \\ \varepsilon_{12} \end{Bmatrix} \quad (3)$$

where c_{ij} are the stiffness coefficients which can be derived from G and λ. At elastic state, the specified damage variables d_i are equal to 0.

The 3D Hashin's failure criterion accounting for fiber failure and matrix failure is embedded in ABAQUS using subroutine-VUMAT. In this part, two failure models, tensile failure and compressive failure, are mainly considered for the fiber with related damage variables which can be expressed as [34-35]:

$$\text{Tensile failure of fiber,}\ d_{ft} = 1: \begin{cases} \left(\dfrac{\sigma_{11}}{X_T}\right)^2 + \left(\dfrac{\sigma_{12}}{S_{12}}\right)^2 + \left(\dfrac{\sigma_{13}}{S_{13}}\right)^2 \geq 1 \\ \sigma_{11} > 0 \end{cases} \quad (4)$$

$$\text{Compressive failure of fiber,}\ d_{fc} = 1: \begin{cases} \left|\dfrac{\sigma_{11}}{X_C}\right| \geq 1 \\ \sigma_{11} < 0 \end{cases} \quad (5)$$

where d_{ft} and d_{fc} are the damage variables for evaluating tensile failure and compressive damage of fiber, respectively.

Similarly, tensile failure and compressive failure of the matrix can also be obtained [34-35].

$$\text{Tensile failure of matrix,}\ d_{mt} = 1: \begin{cases} \left(\dfrac{\sigma_{11}}{X_T}\right)^2 + \left(\dfrac{\sigma_{12}}{S_{12}}\right)^2 + \left(\dfrac{\sigma_{22}}{Y_T Y_C}\right)^2 + \dfrac{\sigma_{22}}{Y_T} + \dfrac{\sigma_{22}}{Y_C} \geq 1 \\ \sigma_{22} + \sigma_{33} > 0 \end{cases} \quad (6)$$

$$\text{Compressive failure of matrix,}\ d_{mc} = 1: \begin{cases} \left(\dfrac{\sigma_{11}}{X_T}\right)^2 + \left(\dfrac{\sigma_{12}}{S_{12}}\right)^2 + \left(\dfrac{\sigma_{22}}{Y_T Y_C}\right)^2 + \dfrac{\sigma_{22}}{Y_T} + \dfrac{\sigma_{22}}{Y_C} \geq 1 \\ \sigma_{22} + \sigma_{33} < 0 \end{cases} \quad (7)$$

where d_{mt} and d_{mc} are the damage variables for evaluating tensile failure and compressive damage of matrix, respectively.

Using the damage variables and related parameters, the stress is decreased linearly to zero once the failure criterion is reached. The stiffness coefficients obtained from Equation 3 should be re-calculated during damage process, as:

$$c_{11} = E_1\left(1-\upsilon_{23}\upsilon_{32}\right)\Gamma\left(1-d_f\right) \quad (8a)$$

$$c_{22} = E_2\left(1-\upsilon_{13}\upsilon_{31}\right)\Gamma\left(1-d_f\right)\left(1-d_m\right) \quad (8b)$$

$$c_{33} = E_3\left(1-\upsilon_{12}\upsilon_{21}\right)\Gamma\left(1-d_f\right)\left(1-d_m\right) \quad (8c)$$

$$c_{12} = E_1\left(\upsilon_{21}+\upsilon_{31}\upsilon_{23}\right)\Gamma\left(1-d_f\right)\left(1-d_m\right) \quad (8d)$$

$$c_{23} = E_2\left(\upsilon_{32}+\upsilon_{12}\upsilon_{31}\right)\Gamma\left(1-d_f\right)\left(1-d_m\right) \quad (8e)$$

$$c_{13} = E_1\left(\upsilon_{31}+\upsilon_{21}\upsilon_{32}\right)\Gamma\left(1-d_f\right)\left(1-d_m\right) \quad (8f)$$

$$c_{44} = E_{12}\left(1-d_f\right)\left(1-s_{mt}d_{mt}\right)\left(1-s_{mc}d_{mc}\right) \quad (8g)$$

$$c_{55} = E_{23}\left(1-d_f\right)\left(1-s_{mt}d_{mt}\right)\left(1-s_{mc}d_{mc}\right) \quad (8h)$$

Preprints (www.preprints.org) | NOT PEER-REVIEWED | Posted: 7 November 2018 doi:10.20944/preprints201811.0180.v1

Peer-reviewed version available at Materials 2018, 12, 7; doi:10.3390/ma12010007

$$c_{66} = E_{13}\left(1-d_f\right)\left(1-s_{mt}d_{mt}\right)\left(1-s_{mc}d_{mc}\right) \quad (8i)$$

$$\Gamma = 1/\left(1-\upsilon_{12}\upsilon_{21}-\upsilon_{23}\upsilon_{32}-\upsilon_{13}\upsilon_{31}-2\upsilon_{21}\upsilon_{32}\upsilon_{13}\right) \quad (8j)$$

where s_{mt} and s_{mc} are the factors that control the reduction in shear stiffness according to tensile and compressive failure, respectively. Parameters $d_f = 1-\left(1-d_{ft}\right)\left(1-d_{fc}\right)$ and $d_m = 1-\left(1-d_{mt}\right)\left(1-d_{mc}\right)$ are the global damage variables charactering fiber and matrix, respectively.

Table 1. Material parameters of unidirectional glass fiber/epoxy composite laminates.

Mechanical constants	Values
Young's modulus/GPa (E_1, E_2, E_3)	55.2,18.4,18.4
Poisson's ratio (ν_{12}, ν_{13}, ν_{23})	0.27,0.27,0.43
Shear modulus/GPa (E_{12}, E_{13}, E_{23})	13.8, 13.8, 13.8
Ultimate tensile stress/MPa (X_T, Y_T, Z_T)	1656, 73.8,73.8
Ultimate compressive stress/MPa (X_C, Y_C, Z_C)	1656, 91.8,91.8
Ultimate shear stress/MPa (S_{12}, S_{13}, S_{23})	117.6, 117.6,117.6

2.2. Material property of SMA

A similar stress-strain relationship as Equation 1 can be observed if the reinforced material is isotropic elastic, i.e. glass fiber or carbon fiber. Differently, the constitutive model of SMA is sensitive to temperature and stress state. Brinson's model [36-37] has been referred to most often in subsequent studies due to its high accuracy. Here, the constitutive law of SMA based on energy balance equations is derived considering the effect of temperature T and phase conversion between martensite and austensite can be denoted as:

$$d\sigma_s = E_s\left(\varepsilon_s,\xi,T\right)d\varepsilon_s + \Omega\left(\varepsilon_s,\xi,T\right)d\xi + \Theta\left(\varepsilon_s,\xi,T\right)dT \quad (9)$$

where σ_s and ε_s are the Piola-Kirchhoff stress and Green strain of SMA; ξ is the martensite fraction charactering the phase conversion; also, E_s , Ω and Θ are the elastic modulus, transformation coefficient and thermal coefficient, respectively.

Some assumptions are taken to simplify the application, as follows: the elastic modulus D is a function of martensite fraction ξ; the transformation coefficient is also connected with elastic modulus:

$$E_s\left(\varepsilon,\xi,T\right) = E_s\left(\xi\right) = E_a + \xi\left(E_m - E_a\right) \quad (10a)$$

$$\Omega\left(\xi\right) = -\varepsilon_L E\left(\xi\right) \quad (10b)$$

where E_m and E_a are elastic moduli for martensite and austenite state, ε_L is the maximum residual strain. The equations of the phase conersion between martensite and austenite can be expressed as (determined by temperature and stress):

(a) Phase conversion to martensite

If $T > M_s$ and $\sigma_s^{cr} + C_m\left(T-M_s\right) < \sigma < \sigma_f^{cr} + C_m\left(T-M_s\right)$

$$\xi_S = \frac{1-\xi_{S_0}}{2}\cos\left\{\frac{\pi}{\sigma_s^{cr}-\sigma_f^{cr}}\left(\sigma-\sigma_f^{cr}-C_m\left(T-M_s\right)\right)\right\} + \frac{1+\xi_{S_0}}{2} \quad (11a)$$

$$\xi_T = \xi_{T_0} - \frac{\xi_{T_0}}{1-\xi_{S_0}}\left(\xi_S - \xi_{S_0}\right) \quad (11b)$$

If $T < M_s$ and $\sigma_s^{cr} < \sigma < \sigma_f^{cr}$

$$\xi_S = \frac{1-\xi_{S_0}}{2}\cos\left\{\frac{\pi}{\sigma_s^{cr}-\sigma_f^{cr}}\left(\sigma-\sigma_f^{cr}\right)\right\} + \frac{1+\xi_{S_0}}{2} \quad (11c)$$

Preprints (www.preprints.org) | NOT PEER-REVIEWED | Posted: 7 November 2018 doi:10.20944/preprints201811.0180.v1

Peer-reviewed version available at *Materials* **2018**, *12*, 7; doi:10.3390/ma12010007

$$\xi_T = \xi_{T_0} - \frac{\xi_{T_0}}{1-\xi_{S_0}}\left(\xi_S - \xi_{S_0}\right) + \Delta_{T\xi} \tag{11d}$$

$$\Delta_{T\xi} = \begin{cases} \frac{1-\xi_{T_0}}{2}\left[\cos\left(a_m\left(T-M_f\right)\right)+1\right] : M_f < T < M_s \text{ and } T < T_0 \\ 0 : \text{else} \end{cases} \tag{11e}$$

(b) Phase conversion to austenite

If $T > A_s$ and $C_a\left(T-A_f\right) < \sigma < C_a\left(T-A_s\right)$

$$\xi = \frac{\xi_0}{2}\left\{\cos\left[a_a\left(T-A_s-\frac{\sigma}{C_a}\right)\right]+1\right\} \tag{12a}$$

$$\xi_S = \xi_{S_0} - \frac{\xi_{S_0}}{\xi_0}\left(\xi_0-\xi\right) \tag{12b}$$

$$\xi_T = \xi_{T_0} - \frac{\xi_{T_0}}{\xi_0}\left(\xi_0-\xi\right) \tag{12c}$$

In Equation 11 and 12, parameters $a_m = \pi/\left(M_s - M_f\right)$ and $a_a = \pi/\left(A_f - A_s\right)$. Four important parameters are introduced to character the phase conversion temperature: M_s - start temperature of martensite phase; M_f -finish temperature of martensite phase; A_s - start temperature of austenite phase; A_f - finish temperature of austenite phase. The stress-strain relationship at arbitrary temperature T can be obtained according to Equation 9-12. Debonding behavior of interface between SMA and matrix is carried out by use of cohesive zone model.

2.3. Material property of interphase

According to our research in glass fiber reinforced polymer composite, the time (or strain rate) depended stress-strain relationship has been investigated [33]. In this model, the time affect is existing in interphase part and can be expressed as stress $\sigma_{in,ij}(t)$ to strain relationship experiencing some continuous strain history given by the function $\sigma_{in,ij}(t)$:

$$\sigma_{in}(t) = \int_0^t g\left(t-t'\right)\dot{\varepsilon}_{in}\left(t'\right)dt' \tag{13}$$

where g is the relaxation modulus, t' is new time variable, $\dot{\varepsilon}_{in}(t) = \partial\varepsilon_{in}(t')/\partial t'$ is strain rate. The strain history $\varepsilon_{in}(t)$ can be obtained using Boltzmann superposition principle. Also, the relaxation modulus g can be expressed using discrete relaxation spectrum as follows:

$$g(t) = g_0 + \sum_{i=1}^{n} g_i e^{\frac{-t}{t_i}} \tag{14}$$

where g_0, g_i and t_i are the related parameters which can be obtained from relaxation tests. The parameters in interphase part can be obtained by fitting with tensile or pull-put tests with different loading speed [33].

2.4. Boundary condition

For a sample with dimension $L_x \times L_y \times L_z = 100\text{mm} \times 100\text{mm} \times \left(n \times 0.2\text{mm}\right)$, n=16 for our experiment, the fixed boundary is employed to investigate the accuracy of numerical model. Frequency and amplitude of the four boundaries $x=0$, $x=L_x$, $y=0$ and $y=L_x$ are zero, and shown in Figure 1a.

 doi:10.20944/preprints201811.0180.v1

Peer-reviewed version available at *Materials* **2018**, *12*, 7; doi:10.3390/ma12010007

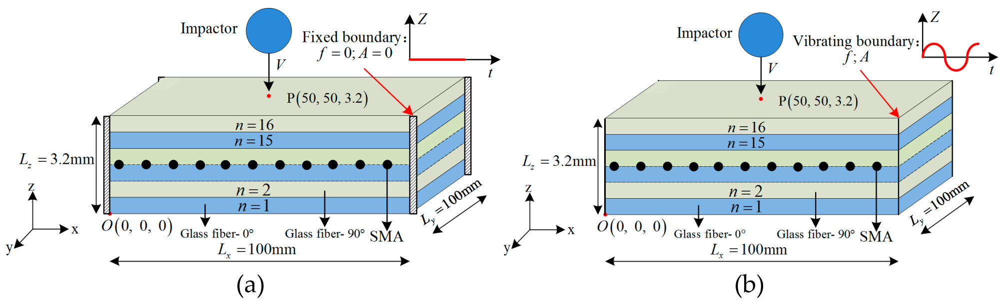

Figure 1. Schematic of the SMA reinforced composite samples: (a) Fixed boundary; (b) Vibrating boundary.

As for vibrating boundary condition (Figure 1b), the movement of the boundaries can be expressed as:

$$z = A\sin\left(2\pi ft\right) \tag{13}$$

where A and f are the amplitude and the frequency of the vibration, respectively.

3. Effect of fixed boundary condition on impact resistance

The fixed boundary condition is kept in the experiment process.

3.1. Composite laminates

Simulation results of the model under fixed boundary are investigated and compared with the experimental results. Stacking sequence of the laminate is $[0^{o},90^{o}]_{8}$, 0o and 90o are the layer angles (glass fiber) to X- direction. The sample ($L_x \times L_y \times L_z$ = 100mm×100mm×3.2mm) is impacted by a rigid half ball-cylinder on the center of the top surface, as shown in Figure 1. Diameter of the half ball of the impactor is 14mm, and the mass of the impactor is 8kg (Steel). Two impact energies are considered in the tests, 32J and 64J, and the corresponding impact velocities are 2.83m/s and 4m/s. The SMA wires (diameter 0.2mm) have been embedded in the middle layer laminate (between layer 8 and 9) with distance 5mm (total 21 wires for a model). In summary, four types of experiments have been conducted, as shown in Table 2.

Table 2. Experimental groups.

	Stacking sequence	Impact energy/J
Group A1	$[0^{o},90^{o}]_{8}$	32
Group A2	$[0^{o},90^{o}]_{8}$	64
Group A3	$[(0^{o},90^{o})_{4}$,SMA, $(0^{o},90^{o})_{4}]$	32
Group A4	$[(0^{o},90^{o})_{4}$,SMA, $(0^{o},90^{o})_{4}]$	64

3.2. Simulation result: damage state during impact process

The model has been built in ABAQUS according to the details mentioned before, as shown in Figure 2.

Preprints (www.preprints.org) | NOT PEER-REVIEWED | Posted: 7 November 2018 doi:10.20944/preprints201811.0180.v1

Peer-reviewed version available at *Materials* **2018**, *12*, 7; doi:10.3390/ma12010007

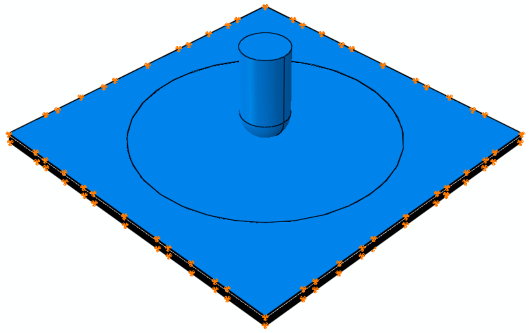

Figure 2. Modeling the impact test of the composite laminate.

Group A1: The simulation results of the composite laminate under impact at different time (0.0015 s < *t* < 0.009 s) are shown in Figure 3 and Figure 4. Under lower impact energy, 32J, a generally elastic behavior of the composite laminate can be drawn as: deformation is increased with time t from initial state (*t* = 0) to the maximum deformation (*t* ≈ 0.0045s), then the deformation is decreased.

As shown in Figure 3, it is clear that the impactor has been bounced back by the composite laminate. Three layers have been chosen to investigate the fracture morphology during impact as shown in Figure 4: layer 16, 8 and 1. A hole shape damage can be founded on several layers, especially layer 16, however the damage region on the layer 8 and layer 1 are smaller, as shown in Figure 4.

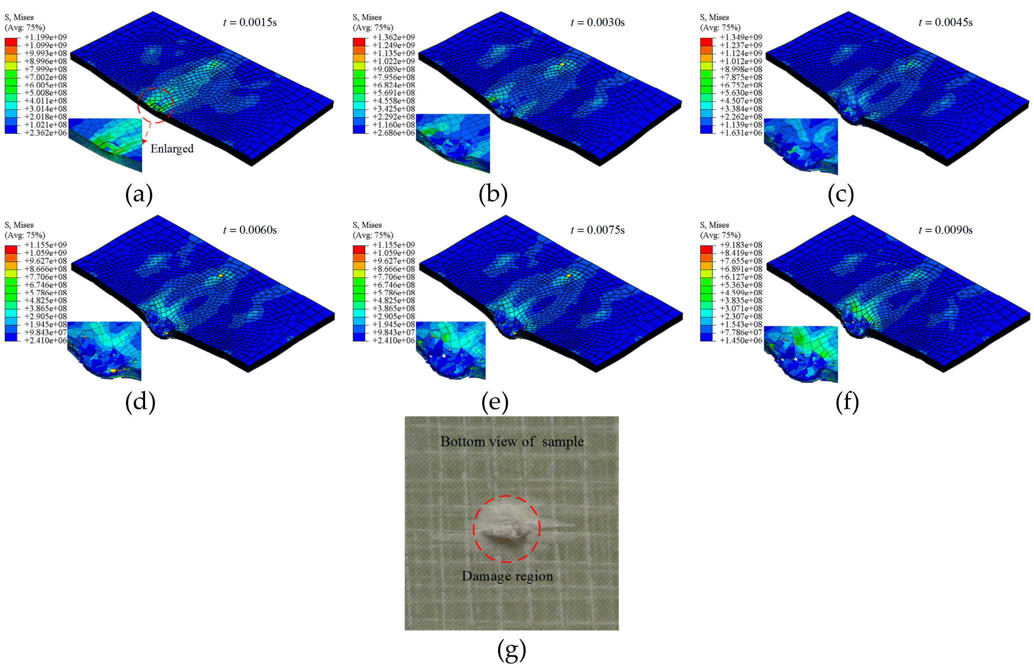

Figure 3. Simulation results of the composite laminates at different time, group A1. and the bottom view of the real sample after impact.

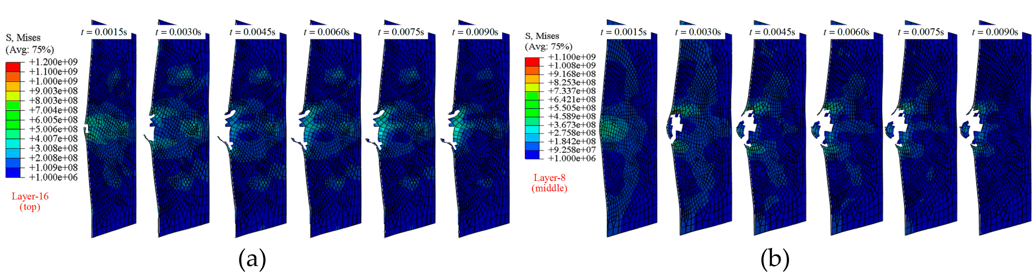

Preprints (www.preprints.org) | NOT PEER-REVIEWED | Posted: 7 November 2018 doi:10.20944/preprints201811.0180.v1

Peer-reviewed version available at *Materials* **2018**, *12*, 7; doi:10.3390/ma12010007

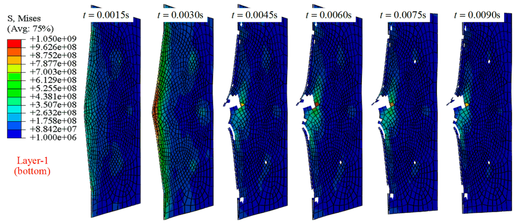

(c)

Figure 4. Cross-section of different layers during impact, group A1: (a) layer 16; (b) layer 8; (c) layer 1.

Group A2: Different from group A1, the composite is destroyed completely under higher energy, 64J, as shown in Figure 5. During simulation process, the impactor is founded moving along the top layer to the bottom layer of the composite without bounced back (t > 0.0030s), this can also be confirmed by the experimental result, as shown in Figure 5g. The velocity of impactor is reduced in the breakdown process then remained as a constant.

From Figure 6c, a larger damage region is founded at the final state. This is different from group A1, and can be explained by delamination due to the friction between impactor and layer 1 during penetration.

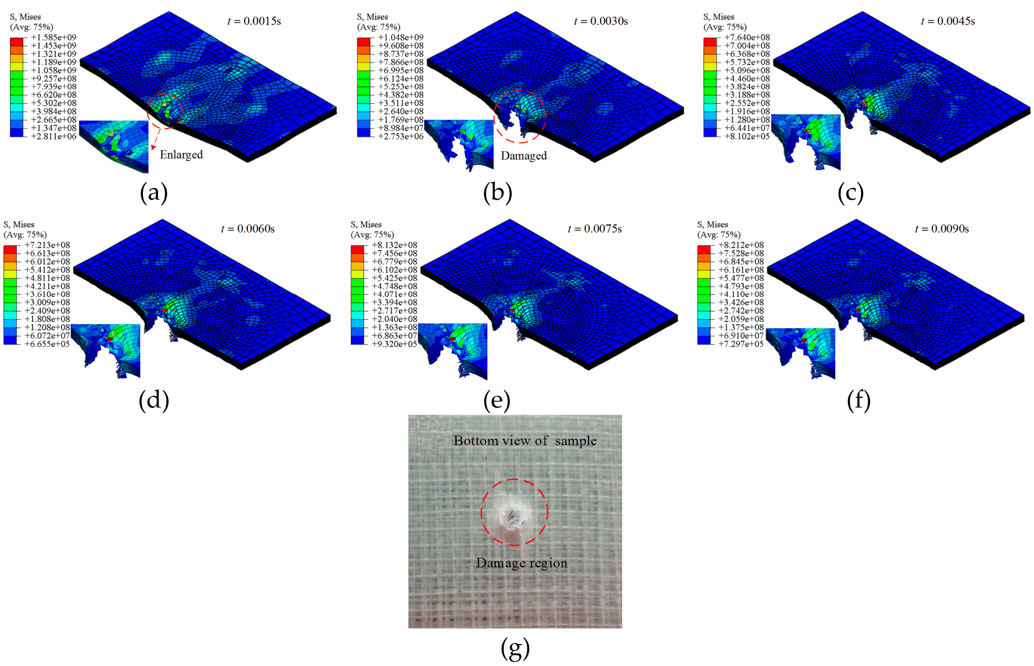

Figure 5. Simulation results of the composite laminates at different time, group A2.

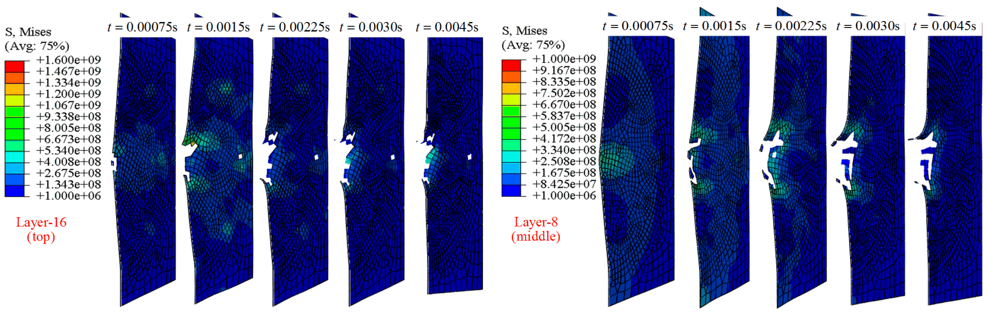

(a) (b)

Preprints (www.preprints.org) | NOT PEER-REVIEWED | Posted: 7 November 2018 doi:10.20944/preprints201811.0180.v1

Peer-reviewed version available at *Materials* **2018**, *12*, 7; doi:10.3390/ma12010007

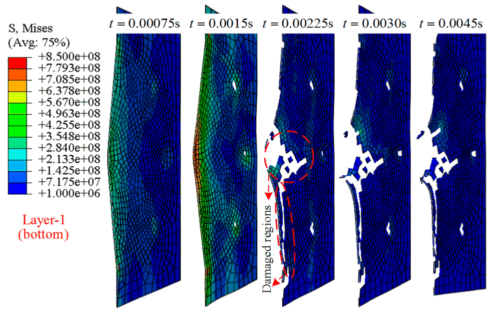

(c)

Figure 6. Cross-section of different layers during impact, group A2: (a) layer 16; (b) layer 8; (c) layer 1.

Group A3 and A4: Embedding SMA alloys is effective to improve the impact resistance of composite laminates. As shown in Figure 7a, SMAs was stretched to a larger strain in the case of 32J. In Figure 7b, a broken or invalid state of SMA is obtained due to the larger strain which is beyond critical value. More specific, 5 SMAs in the center region are chosen to demonstrate the working mechanism, as shown in Figure 8c and 8d.

Beyond that, the defect is obviously: the damage region of layer 8 (contact with SMA) is larger than that of group A1 and A2, as shown in Figure 8a and 8b.

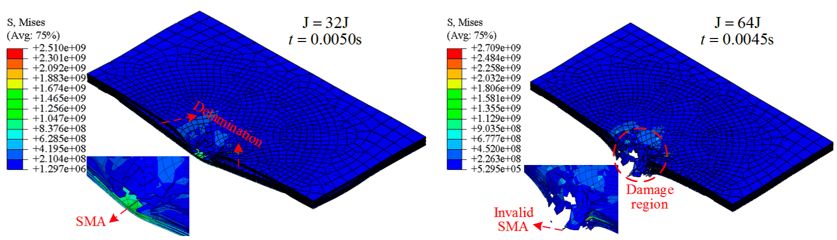

(a) (b)

Figure 7. Simulation results of the SMA reinforced composite laminates at different time: (a) group A3, t = 0.0050s; (b) group A4, t = 0.0045s.

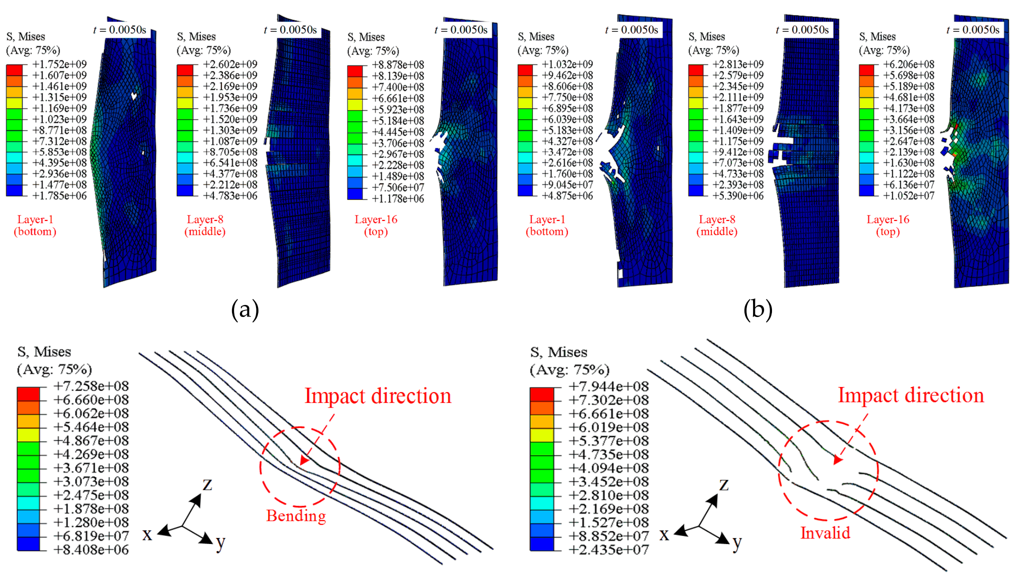

(a) (b)

(c) (d)

Figure 8. Cross-section of different layers during impact: (a) layers in group A3; (b) layers in group A4; (c) SMA in group A3; (d) SMA in group A4.

Preprints (www.preprints.org) | NOT PEER-REVIEWED | Posted: 7 November 2018 doi:10.20944/preprints201811.0180.v1

Peer-reviewed version available at Materials 2018, 12, 7; doi:10.3390/ma12010007

3.3. Simulation result: absorbed energy and contact force

Two important items: absorbed energy and contact force was obtained from ABAQUS and compared with experimental data, as shown in Figure 9. The relative errors of energy comparison are 5.7%, 6.3%, 13.8% and 7.3% for groups A1-A4, respectively. As for the force-time curves, more inflection points are founded on the simulation curves due to the broken and deletion of the element. Even so, the tendency of simulation curves agrees well with the experimental curves. The relative errors for force comparison are 7.3%, 8.1%, 8.9% and 9.2% for groups A1-A4, which can be also accepted.

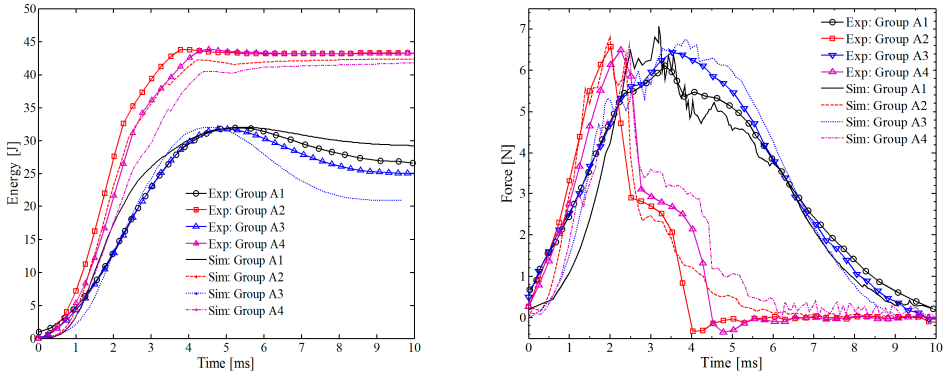

(a) (b)

Figure 9. Comparison between the simulation results and experimental results. (a) absorbed energy-time history; (b) contact force-time history.

From the comparison in this section, the accuracy of material parameters and model used in ABAQUS can be tested. Furthermore, the constitutive relationship of SMA and the processing of interface (between SMA and laminates) are also regarded as appropriate. This is the foundation of the numerical simulation in section 4.

4. Effect of vibrating boundary condition on impact resistance

The simulation of the model under vibrating boundary under impact is investigated in this section. The same model ($L_x \times L_y \times L_z$ = 100mm×100mm×3.2mm, 16 layers) is impacted by a rigid half ball-cylinder with a fixed energy 32J on the center of the top layer as shown section 3.1. Two types of composites have been invested: without SMA and with SMA.

4.1. Effect of amplitude

In order to fully understand the influence of amplitude on the impact resistance, a low frequency f = 1000 cycle/s is kept (10 cycles during simulation process, t_{tot} = 0.01s). Several amplitudes, A, are chosen for the study as shown in Table 3.

Table 3. The amplitudes and frequencies used in the simulation.

	Group B1	Group B2	Group B3	Group B4	Group B5	Group B6	Group B7	Group B8
A(m)	0.0016	-0.0016	0.0032	-0.0032	0.008	-0.008	0.016	-0.016
f(c/s)	1000							
SMA	NO							
Stacking	$[0^{o},90^{o}]_8$							

	Group C1	Group C2	Group C3	Group C4
A(m)	0.0016	0.0032	0.008	0.016
f(c/s)	1000			
SMA	YES			

Preprints (www.preprints.org) | NOT PEER-REVIEWED | Posted: 7 November 2018 doi:10.20944/preprints201811.0180.v1

Peer-reviewed version available at Materials 2018, 12, 7; doi:10.3390/ma12010007

Stacking			[(0°,90°)$_4$, SMA, (0°,90°)$_4$]		
	Group D1	Group D2	Group D3	Group D4	Group D5
A(m)			0.0032		
f (c/s)	100	200	500	2000	10000
SMA			NO		
Stacking			[0°,90°]$_8$		
	Group E1	Group E2	Group E3	Group E4	Group E5
A(m)			0.0032		
f (c/s)	100	200	500	2000	10000
SMA			YES		
Stacking			[(0°,90°)$_4$, SMA, (0°,90°)$_4$]		

The positive value in Table 3 means that the moving direction of the boundary is on the contrary of the impactor's moving direction (+z direction) at initial state. The negative value means that moving directions of impactor and boundary are same at initial time.

When applying amplitude A to control the movement of the boundary, the morphologies of composite laminate after impact are shown in Figure 10 and 11. As shown in Figure 10a, the damage region is close to the size of impactor. From Figure 11b-11d, the damage regions are increased with increasing of the value of applied amplitude, however, general damage with larger area can be observed in case of A=0.016m, as shown in Figure 10d. It is interesting that the damage state is depends on the absolute value of amplitude rather that the valuence when comparing related groups, i.e. Figure 10b and Figure10f. Similar conclusion can be obtained for group C from the simulation results shown in Figure 11.

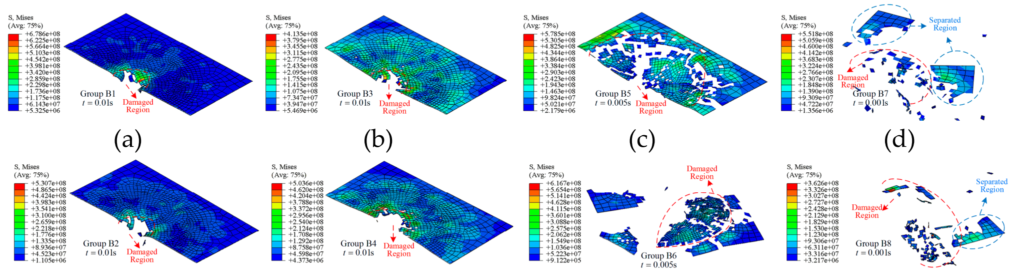

Figure 10. Fracture morphology of the top layer of composite laminate under different amplitudes, group B.

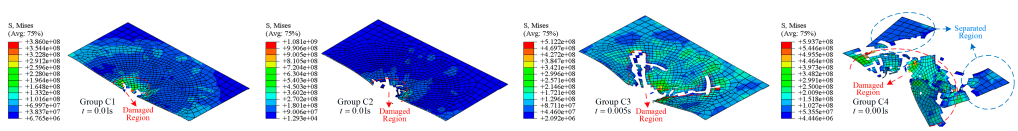

Figure 11. Fracture morphology of top layer of composite laminate with SMA under different amplitudes, group C.

The details of impact process of half model in group B are shown in Figure 12. From Figure 12a, a representative impact process is shown: gradually damage with time t similar with group A1. With increasing amplitude, more elements in the center region have been deleted due to the large deformation (or severe vibration), as shown in Figure 12b, 12c and 12d. As for larger amplitude, 0.016m, a larger damage region is observed, even separating from the main model, t = 0.001s, as shown in Figure 12d. More importantly, the time that the clear damage region can be observed has changed from t = 0.005s to 0.0002s due to the relative movement. The effect of valuence of amplitudes can be further validated comparing Figure 12b and 12e.

Peer-reviewed version available at *Materials* **2018**, *12*, 7; doi:10.3390/ma12010007

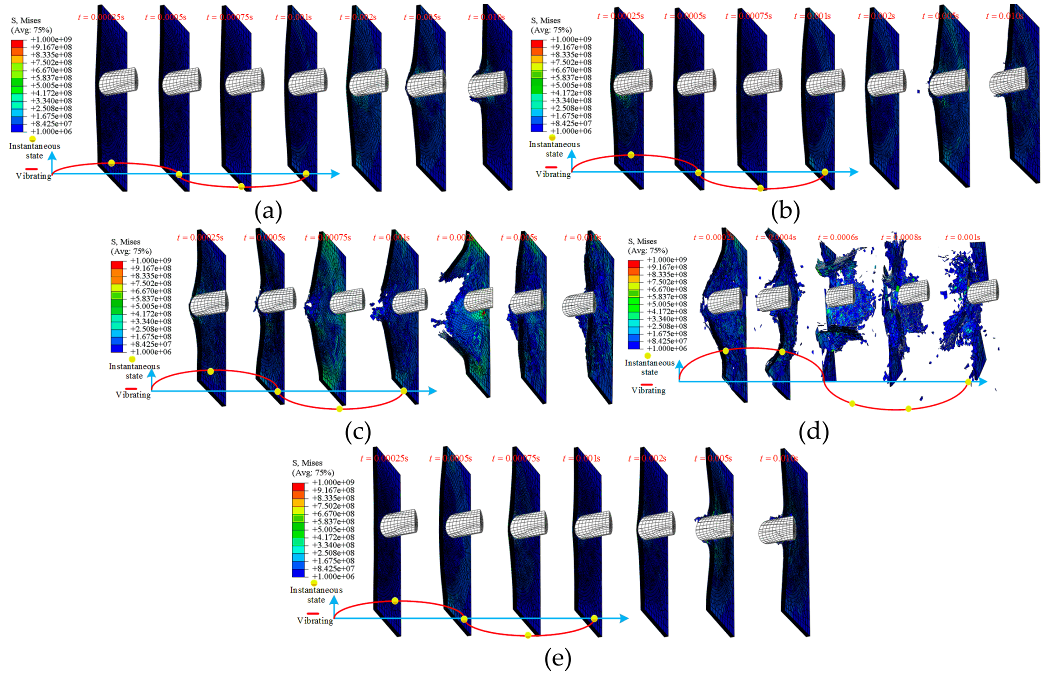

Figure 12. Cross-section of half model during impact: (a) group B1; (b) group B3; (c) group B5; (d) group B7; (e) group B4.

Three amplitudes are shown to demonstrate the impact process of group C: A = 0.0032m, 0.008m and 0.016m, as shown in Figure 13. From Figure 13a, the layer damage along the SMA direction is founded during impact process. This is due to the weak impact resistance of laminate after separating from SMA, especially for layer 8. With increasing amplitude, a clear delamination can be observed between layer 8 and 9, t = 0.0005s, as shown in Figure 13b. As for group C4, a clearly damage is shown at early time, t = 0.0004s. The damage state is still extending even after separating,due to the vibrating of the boundary, as shown in Figure 13c.

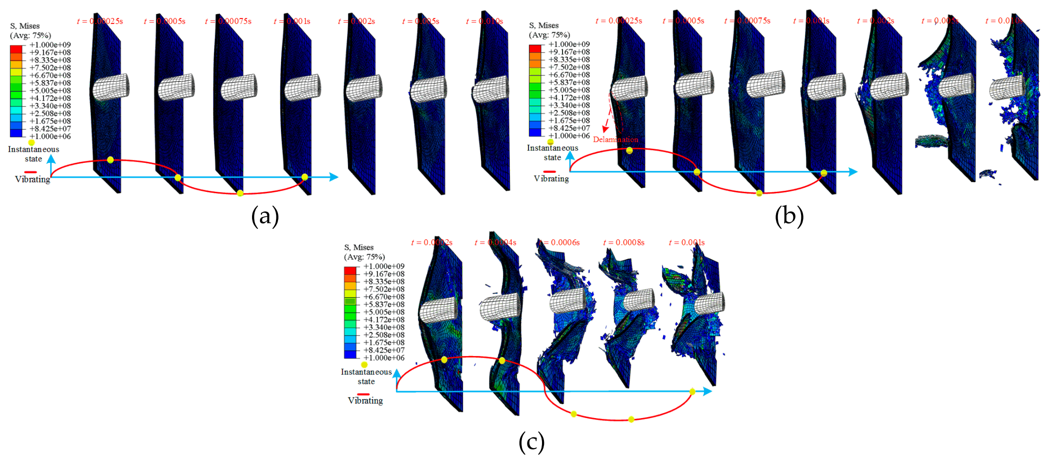

Figure 13. Cross-section of half model during impact: (a) group C2; (b) group C3; (c) group C4.

Preprints (www.preprints.org) | NOT PEER-REVIEWED | Posted: 7 November 2018 doi:10.20944/preprints201811.0180.v1

Peer-reviewed version available at Materials 2018, 12, 7; doi:10.3390/ma12010007

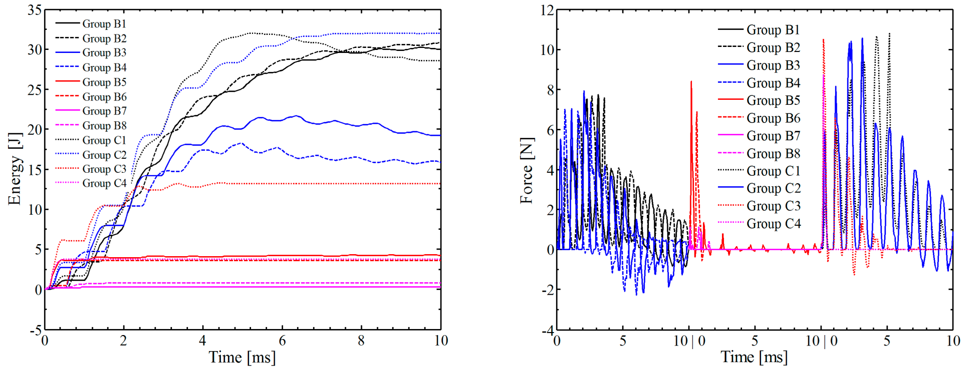

(a) (b)

Figure 14. Analysis of the impact resistance of composite laminate in group B and C: (a) absorbed energy; (b) contact force.

With different amplitudes, the absorbed energy and contact force are plotted against time, as shown in Figure 14. As for group B1 and C1, the maximum value of absorbed energies is 32J, however, the values at t = 0.01s are 30.04J and 28.6J, respectively. With increasing the value of amplitude the absorbed energy is decreased. As for group B3, B5 and B7, the maximum value of absorbed energies are 9.24J, 4.24J and 0.30J, respectively. The maximum value of absorbed energies in related opposite direction groups, i.e. B4, B6 and B8, kept as same level and about 20% lower. As for related group C, the absorbed energy is 3.5 times larger. As for high amplitude, the absorbed energy is close to zero, as group B7 and B8. From t =0 to 0.004s, effect of vibrations on the energy-time curve can be observed, then, the energy is kept as constant, as shown in Figure 14a. In Figure 14b, the force is also affected by the vibration and shown more dramatic changes comparing with section 3.

4.2. Effect of frequency

In order to fully understand the influence of frequency on the impact resistance, a small amplitude A = 0.0032m is kept considering the small influence of this level. Several frequencies, f, are chosen for the study as shown in Table 3.

During the simulation f = 100 cycle/s to 500 cycle/s in group D1 to D3, the damage state is close to each other at time t = 0.01s, only a small hole can be founded according to the fracture morphology shown in Figure 15a, 16b and 16c. As for higher frequency f = 2000 cycle/s to 10000/s, the damage states show randomicity with larger area, as shown in Figure 15d and 16e.

Damage states of SMA reinforced composite laminates are shown in Figure 15f to 15j, also. Overall, the effect of frequency on the damage state is similar with that in group D. It should be noted that the separated region in group E5 maintains a more complete shape, as shown in Figure 15j.

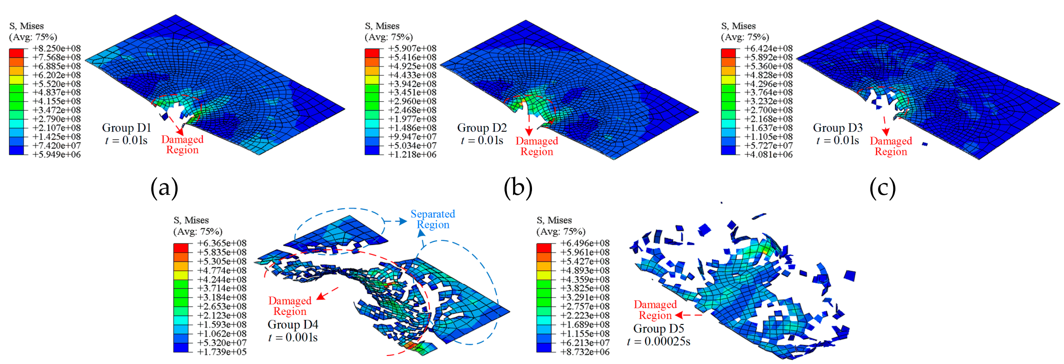

(a) (b) (c)

(d) (e)

Preprints (www.preprints.org) | NOT PEER-REVIEWED | Posted: 7 November 2018 doi:10.20944/preprints201811.0180.v1

Peer-reviewed version available at *Materials* **2018**, *12*, 7; doi:10.3390/ma12010007

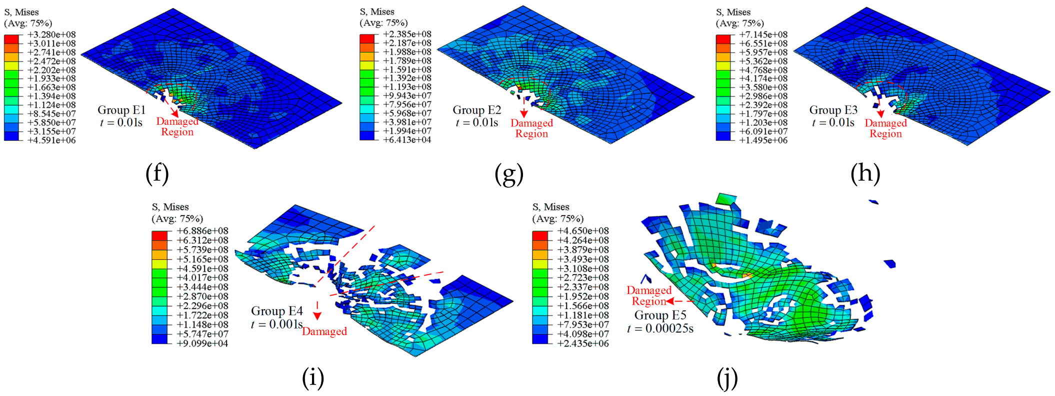

Figure 15. Fracture morphology of the top layer with different frequencies.

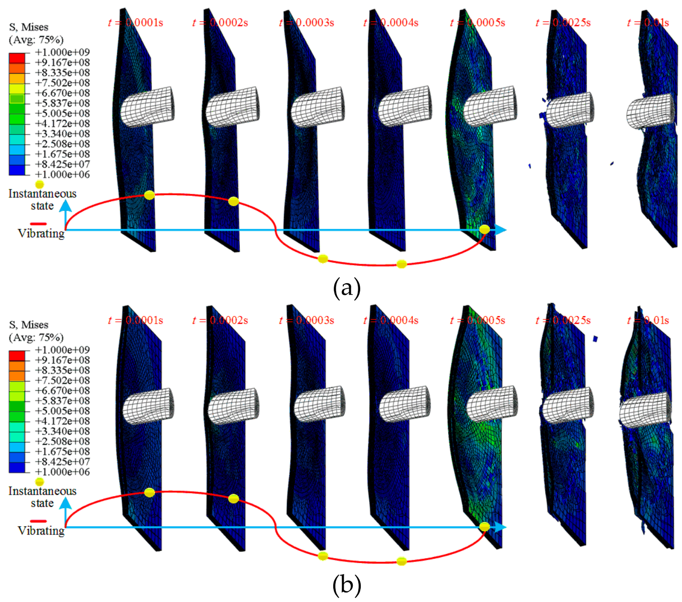

Figure 16. Cross-section of half model during impact: (a) group D4; (b) group E4.

Applying different frequencies f on the boundary, the simulation process of two groups: D5 and E5 are invested to demonstrate the details of damage morphologies of the composite laminate, as shown in Figure 16. As for D4, an hole shape damage region is gradually appear at time t = 0.0025s, then increased with impact process, at time t = 0.01s the center region is damaged completely. As for group E5, delamination is observed except the hole shape damage, this is mainly due to the global enhancement effect of SMA.

The relationship between absorbed energy and time or contact force and time can be founded in Figure 17. As shown in Figure 17a, the absorbed energy is decreased with increasing frequency generally. Considering a real low frequency f =100/s, the maximum value of absorbed energy for group D1 and E1 are same, 32J. Considering a high frequency f = 10000/s, the absorbed energy for group E5 is 2.36J, as for D5 the absorbed energy is 1.79J, which means the composites can barely bearing impact. As shown in Figure 17b, the maximum value of force in the case of f<2000 cycle/s is under the range 7N to 7.5N for group D, 9N to 12N for group E. As for group D5 and E5, a saltation is observed comparing force with the adjacent groups which is mainly due to the transient change of velocity.

More important, the maximum value of absorbed energy and contact force for SMA reinforced composites is generally 15%-30% larger that than of pure glass fiber reinforced composites under same amplitude or frequency.

Peer-reviewed version available at *Materials* **2018**, *12*, 7; doi:10.3390/ma12010007

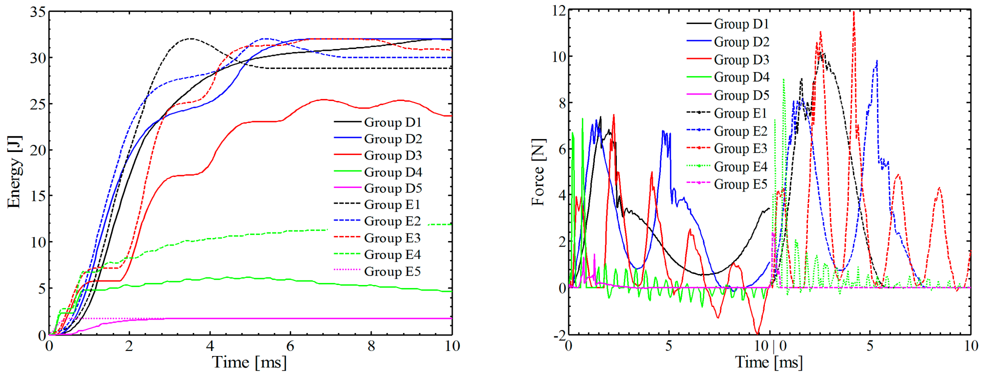

(a) (b)

Figure 17. Analysis of the impact resistance of composite laminate in group D and E: (a) absorbed energy; (b) contact force.

4.3. Statistical analysis of damage state

Table 4. Statistics of absorbed energy and contact force.

	A1	B1	B2	B3	B4	B5	B6	A7	B8
E_{max} (J)	32	32	32	21.67	18.27	4.30	3.72	0.30	0.80
$E_{t=0.01s}$ (J)	28.70	30.04	30.79	9.24	5.90	4.24	3.56	0.30	0.80
F_{max} (N)	7.04	7.74	7.69	7.92	7.35	8.39	6.86	0.86	1.13
F_{avg} (N)	1.93	1.70	1.81	0.83	0.65	0.16	0.13	0.01	0.02

	A3	C1	C2	C3	C4
E_{max} (J)	32	32	32	13.20	3.74
$E_{t=0.01s}$ (J)	25.14	28.60	31.97	13.17	3.74
F_{max} (N)	6.89	10.77	10.56	10.52	8.71
F_{avg} (N)	3.32	2.98	2.31	0.52	0.12

	D1	D2	D3	D4	D5
E_{max} (J)	32	32	25.38	6.21	1.75
$E_{t=0.01s}$ (J)	31.98	31.92	23.68	4.69	1.74
F_{max} (N)	7.40	7.23	7.45	7.29	1.44
F_{avg} (N)	2.31	2.36	1.11	0.17	0.06

	E1	E2	E3	E4	E5
E_{max} (J)	32	32	32	11.86	1.79
$E_{t=0.01s}$ (J)	28.77	29.94	30.70	11.86	1.79
F_{max} (N)	10.15	9.79	11.92	9.02	2.36
F_{avg} (N)	2.95	2.81	2.69	0.46	0.05

In Table 4, the maximum energy- E_{max}, energy at time 0.01s- $E_{t=0.01}$, maximum force- F_{max} and average force- F_{avg} of different groups are shown. Energy E_{max}=32J denotes a rebound behavior of impactor. The average force is defined as:

$$F_{avg} = \frac{\sum_{i=1} F_i}{N} \tag{14}$$

where N is the total number of output data of force F_i within time 0.01s, more important, the average value is still in accordance with A and f.

In Figure 18, the ratio between damaged area and the whole model are plotted against time. Generally, the damaged areas of laminates for $A < 0.0032$m or f <500 cycle/s is kept as < 5%. In Figure 18a, the damaged areas of top layer (layer-16) for $A > 0.0032$m or f >500 cycle/s is kept as 30-50%.

Differently, the damaged area of middle layer (layer-8) and bottom layer (layer-1) under same conditions are kept as 30-70% and 30-65%, respectively.

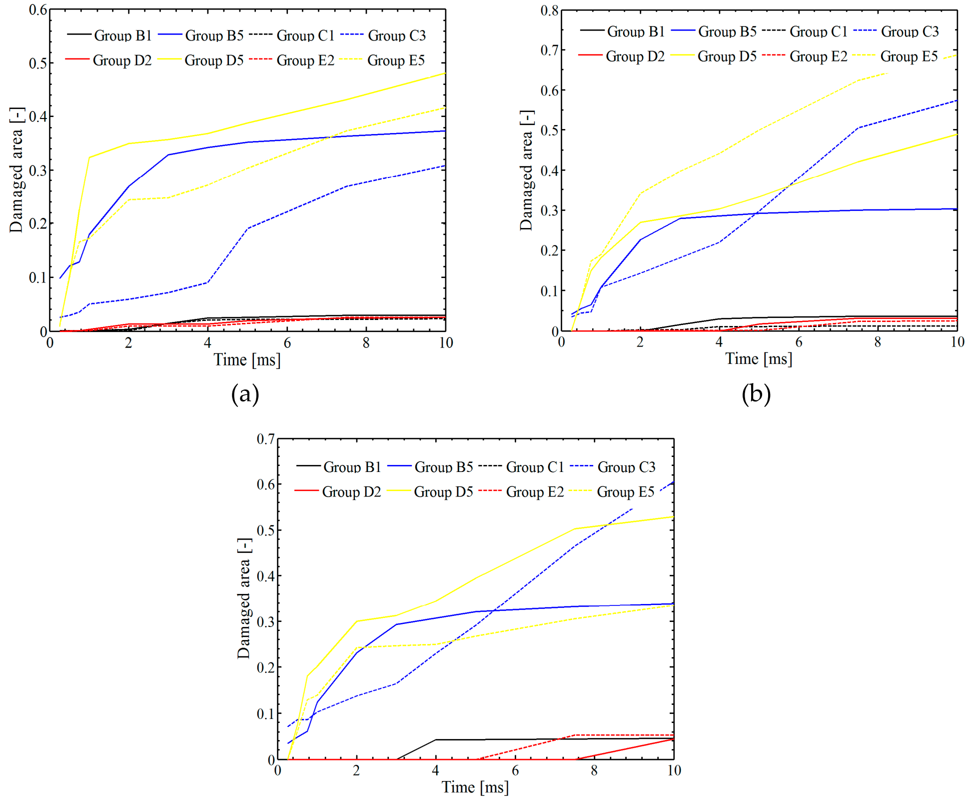

(a) (b)

(c)

Figure 18. Statistic of damage area in different groups: (a) layer-16; (b) layer-8; (c) layer-1.

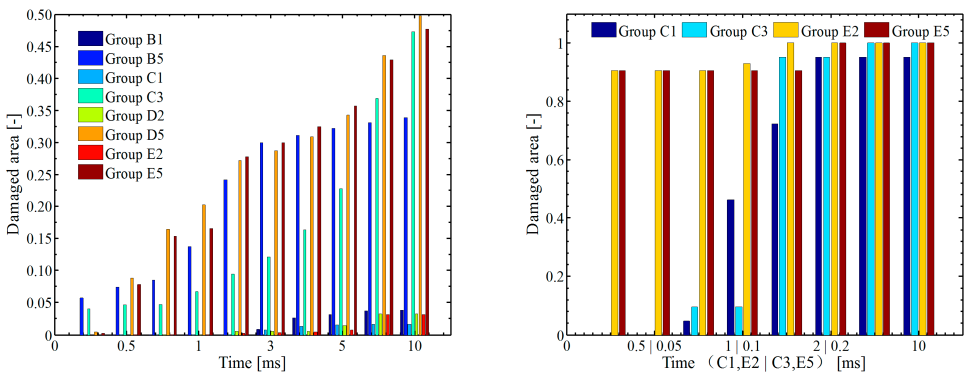

(a) (b)

Figure 19. Statistic of general damage area: (a) laminate; (b) SMA.

In Figure19a, the average damage area are investigated by calculating 16 layers, the results indicate that a 4% damage for small amplitude and frequency and a nearly 50% damage for large amplitude or frequency at time 0.01s. In Figure19b, the damage state of SMA is studied, the damage of SMA can be observed at time earlier than the damage of composite laminates which means that SMA has advantages absorbing energy.

4.4. Mathematical expression-effect of amplitude and frequency

Preprints (www.preprints.org) | NOT PEER-REVIEWED | Posted: 7 November 2018 doi:10.20944/preprints201811.0180.v1

Peer-reviewed version available at *Materials* **2018**, *12*, 7; doi:10.3390/ma12010007

In this section, the relationship between velocity and amplitude (or frequency) is investigated firstly. The results showing a clearly inverse proportion, as:

$$\Delta v = \frac{k_a}{\sum_{i=0} m_i A^i} (\text{for given } f) \quad (15a)$$

$$\Delta v = \frac{k_f}{\sum_{i=0} n_i f^i} (\text{for given } A) \quad (15b)$$

where, where k_a and m_i are parameters related to amplitude; k_f and n_i are parameters related to frequency. Inserting Equation 15 to energy equation, the relationship between absorbed energy and amplitude (or frequency) is obtained as:

$$E = \frac{1}{2} m V_0^2 - \frac{1}{2} m \left(V_0 - \frac{k}{\sum_{i=0} m_i A^i \sum_{i=0} n_i f^i} \right)^2 \quad (16)$$

where E and m is the absorbed energy and mass of the impactor, respectively. Considering that average $F_{avg} = m \times \Delta v / \Delta t$, the average force is also obtained as:

$$F_{avg} = \frac{k}{t_{tot} \sum_{i=0} m_i A^i \sum_{i=0} n_i f^i} \quad (17)$$

The simulation results using the equations mentioned above are shown in Figure 20. In this simulation, i = 3 is chosen to simplify the expression. The comparison indicate that the both energy and force can be predicted using Equation 16 and 17.

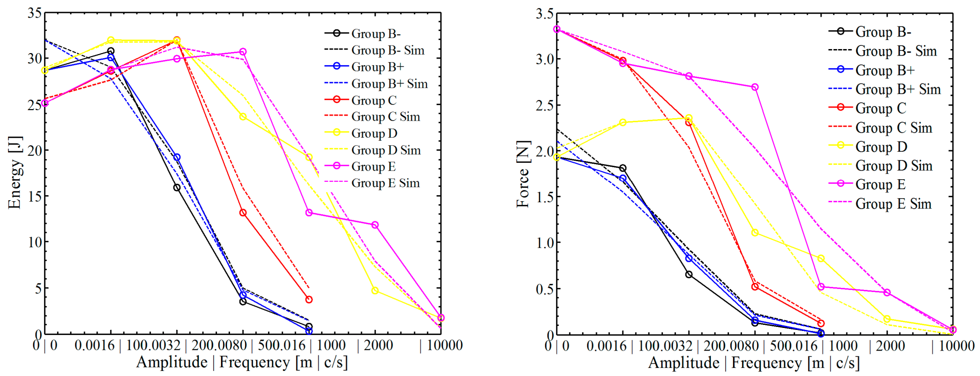

(a) (b)

Figure 20. Comparison study of statistical results and simulation results: (a) energy- $E_{t=0.01}$; (b) force- F_{avg}.

5. Conclusions

The effect of vibrating boundary on the impact resistance of SMA reinforced composite laminates has been investigated. Two main factors are used to charactering the vibration of the boundary: amplitude and frequency. A 3D finite element model based on Hashin's failure criterion was employed in ABAQUS to study the destruction process. A Mathematical expression is obtained to charactering the effect of vibration on energy and force.

Comparison between the simulation results and our previous work with fixed boundary shows that the parameters and the simulation process are acceptable with relative error smaller than 10% (both for 32J and 64J). As for vibrating boundary condition with different amplitudes and frequencies, the absorbed energy and the fracture morphology of the composite laminate have been studied.

- Both high frequency and amplitude can weaken the impact resistance of composite laminate, extensive damage can be observed rather than impact hole.

- The absolute value of amplitude has greater influence on the impact resistance rather than the moving direction of laminates at initial time. The absorbed energy and contact force in positive direction is about 20% larger than that in negative direction.
- Embedding of SMA can improve the impact resistance of composite laminates due to the superelasticity- with increasing absorbed energy and contact force about 50%; also, embedding of SMA can also change the damge morphology: shape and proportion.

Author Contributions: conceptualization, Jian He; methodology, Mengzhou Chang; software, Mengzhou Chang; validation, Min Sun; formal analysis, Mengzhou Chang; investigation, Mengzhou Chang; resources, Min Sun; data curation, Min Sun; writing—original draft preparation, Fangyun Kong; writing—review and editing, Fangyun Kong; visualization, Fangyun Kong; supervision, Jian He; project administration, Jian He; funding acquisition, Jian He.

Funding: This research was funded by National Natural Science Foundation of China, grant number 11872157, 11472086 and 11532013.

Conflicts of Interest: The authors declare no conflict of interest.

References

1. Biron, M. Thermoplastics and thermoplastic composites. 2nd ed. Massachusetts: William Andrew; **2013**.
2. Mallick, P.K. Fiber-reinforced composites: materials, manufacturing, and design. 3rd ed. Florida: CRC Press, **1993**.
3. Mortazavian, S.; Fatemi, A. Effects of fiber orientation and anisotropy on tensile strength and elastic modulus of short fiber reinforced polymer composites. *Compos. Part. B. Eng.* **2015**, 72, 116-129.
4. Mortazavian, S.; Fatemi, A. Fatigue behavior and modeling of short fiber reinforced polymer composites: a literature review, *Int. J. Fatigue.* **2015**, 70(1), 297-321.
5. Thomason, J.L. The influence of fiber properties of the performance of glass- fibre- reinforced polyamide 6,6. *Compos. Sci. Technol.* **1999**, 59, 2315-2328.
6. Thomason, J.L. The influence of fibre length, diameter and concentration on the modulus of glass fibre reinforced polyamide 6,6. *Compos. Part. A.* **2008**, 39, 1732-1738.
7. Thomason, J.L. The influence of fibre length, diameter and concentration on the impact performance of long glass-fibre reinforced polyamide 6,6. *Compos. Part. A.* **2009**, 40, 114-124.
8. Wang, Z.; Zhou, Y.; Mallick, P.K. Effects of temperature and strain rate on the tensile behavior of short fiber reinforced polyamide-6. *Polym. Compos.* **2002**, 23(5), 858-871.
9. Zhou, Y.; Mallick, P.K. A non-linear damage model for the tensile behavior of an injection molded short E-glass fiber reinforced polyamide-6,6. *Mater. Sci. Eng.* A. **2005**, 393(1) 303-309.
10. Cho, H.K.; Rhee, J. Nonlinear finite element analysis of shape memory alloy (SMA) wire reinforced hybrid laminate composite shells. *Int. J. NonLin. Mech.* **2012**, 47(6), 672-678.
11. Brinson, L. One-dimensional constitutive behavior of shape memory alloys: thermomechanical derivation with non-constant material functions and redefined martensite internal variable. *J. Intell. Mater. Sys. Struct.* **1993**, 4, 229-242.
12. Sun, M.; Wang, Z.; Yang, B. Experimental investigation of GF/epoxy laminates with different SMAs positions subjected to low-velocity impact. *Compos. Struct.* **2017**, 171, 170-184.
13. Khalili, S.M.R.; Botshekanan Dehkordi, M.; Carrera, E.; Shariyat, M. Non-linear dynamic analysis of a sandwich beam with pseudoelastic SMA hybrid composite faces based on higher order finite element theory. *Compos. Struct.* **2013**, 96, 243-255.
14. Khalili, S.M.R.; Botshekanan Dehkordi, M.; Shariyat, M. Modeling and transient dynamic analysis of pseudoelastic SMA hybrid composite beam. *Appl. Math. Comput.* **2013**, 219, 9762-9782.
15. Shariyat, M.; Hosseini, S.H. Accurate eccentric impact analysis of the preloaded SMA composite plates, based on a novel mixed-order hyperbolic global-local theory. *Compos. Struct.* **2015**, 124, 140-151.
16. Shariyat, M.; Moradi, M.; Samaee, S. Enhanced model for nonlinear dynamic analysis of rectangular composite plates with embedded SMA wires, considering the instantaneous local phase changes. *Compos. Struct.* **2014**, 109, 106-118.
17. Bienias, J.; Jakubczak, P.; Dadej, K. Low-velocity impact resistance of aluminium glass laminates–Experimental and numerical investigation. *Compos. Struct.* **2016**, 152, 339-348.

18. Zhang, R.; Ni, Q.Q.; Natsuki, T. Mechanical properties of composites filled with SMA particles and short fibers. *Compos. Struct.* **2007**, 79(1), 90-96.
19. Chawla, N.; Sidhu, R.S.; Ganesh, V.V. Three-dimensional visualization and microstructure-based modeling of deformation in particle-reinforced composites. *Acta. Mater.* **2006**, 54(6), 1541-1548.
20. Susainathan, J.; Eyma, F.; De Luycker, E. Experimental investigation of impact behavior of wood-based sandwich structure. *Compos. Part. A.* **2018**, 109, 10-19.
21. Shariyat, M. A double-superposition global-local theory for vibration and dynamic buckling analyses of viscoelastic composite/sandwich plates: a complex modulus approach. *Arch. Appl. Mech.* **2011**, 81, 1253-1268.
22. Hart, K.R.; Chia, P.X.L.; Sheridan, L.E. Mechanisms and characterization of impact damage in 2D and 3D woven fiber-reinforced composites. *Compos. Part. A.* **2017**, 101, 432-443.
23. Asaee, Z.; Taheri, F. Experimental and numerical investigation into the influence of stacking sequence on the low-velocity impact response of new 3D FMLs. *Compos. Struct.* **2016**, 140, 136-146.
24. Shariyat, M.; Hosseini, S.H. Eccentric impact analysis of pre-stressed composite sandwich plates with viscoelastic cores: a novel global-local theory and a refined contact law. *Compos. Struct.* **2014**, 117, 333-345.
25. Suzuki, Y.; Suzuki, T.; Todoroki, A. Smart lightning protection skin for real-time load monitoring of composite aircraft structures under multiple impacts. *Compos. Part. A.* **2014**, 67, 44-54.
26. Liu, H.; Falzon, B.G.; Tan, W. Predicting the Compression-After-Impact (CAI) strength of damage-tolerant hybrid unidirectional/woven carbon-fibre reinforced composite laminates. *Compos. Part. A.* **2018**, 105, 189-202.
27. Liu, C.J.; Todd, M.D.; Zheng, Z.L. A nondestructive method for the pretension detection in membrane structures based on nonlinear vibration response to impact. *Struct. Health. Monit.* **2018**, 17(1), 67-79.
28. Zhao, L.; Yang, Y. An impact-based broadband aeroelastic energy harvester for concurrent wind and base vibration energy harvesting. *Appl. Energ.* **2018**, 212, 233-243.
29. Shahdin, A.; Morlier, J.; Mezeix, L. Evaluation of the impact resistance of various composite sandwich beams by vibration tests. *Shock. Vib.* **2013**, 18(6), 789-805.
30. Li, W.; Zheng, H.; Sun, G. The moving least squares based numerical manifold method for vibration and impact analysis of cracked bodies. *Eng. Fract. Mech.* **2017**, 190.
31. Pérez, M.A.; Oller, S.; Felippa, C.A. Micro-mechanical approach for the vibration analysis of CFRP laminates under impact-induced damage. *Compos. Part. B. Eng.* **2015**, 83, 306-316.
32. Miramini, A.; Kadkhodaei, M.; Alipour, A. Analysis of interfacial debonding in shape memory alloy wire-reinforced composites. *Smart. Mater. Struct.* **2015**, 25(1), 015032.
33. Chang, M.; Wang, Z.; Liang, W. A visco-hyperelastic model for short fiber reinforced polymer composites: reinforcement and fracture mechanisms. *Text. Res. J.* **2017**, 0040517517732078.
34. Hashin, Z.; Failure criteria for unidirectional composites. *J. Appl. Mech.* **1980**, 47(2), 329-334.
35. Puck, A.; Schürmann, H. Failure analysis of FRP laminates by means of physically based phenomenological models. *Compos. Sci. Technol.* **1998**, 58(7), 1045-1067.
36. Brinson, L.C.; Lammering, R. Finite element analysis of the behavior of shape memory alloys and their applications. *Int. J. Solids. Struct.* **1993**, 30, 3261-3280.
37. Brinson, L.C. One-dimensional constitutive behavior of shape memory alloys: thermomechanical derivation with non-constant material functions and redefined martensite internal variable. *J. Intel. Mat. Syst. Str.* **1993**, 4, 229-242.